

# In vivo detection of carnosine and its derivatives using chemical exchange saturation transfer

Solène Bardin<sup>1</sup>  | Michele Lecis<sup>1</sup>  | Davide Boido<sup>1</sup> | Céline Boutin<sup>2</sup> |  
Giovanna Baron<sup>3</sup>  | Giancarlo Aldini<sup>3</sup> | Patrick Berthault<sup>2</sup> |  
Fawzi Boumezbaur<sup>1</sup> | Luisa Ciobanu<sup>1</sup> 

<sup>1</sup>NeuroSpin, UMR CEA/CNRS 9027, Paris-Saclay University, Gif-sur-Yvette, France

<sup>2</sup>IRAMIS, NIMBE, UMR CEA/CNRS 3685, Laboratoire Structure et Dynamique par Résonance Magnétique, Gif-sur-Yvette, France

<sup>3</sup>Department of Pharmaceutical Sciences, Medicinal Chemistry Section "Pietro Pratesi", University of Milan, Milan, Italy

## Correspondence

Luisa Ciobanu, Neurospin, CEA, Centre CEA de Saclay, Bat 145, 91191 Gif-sur-Yvette, France.  
Email: luisa.ciobanu@cea.fr

## Funding information

Agence Nationale de la Recherche, Grant/Award Number: ANR-18-CE92-0054-01

**Purpose:** To detect carnosine, anserine and homocarnosine in vivo with chemical exchange saturation transfer (CEST) at 17.2 T.

**Methods:** CEST MR acquisitions were performed using a CEST-linescan sequence developed in-house and optimized for carnosine detection. In vivo CEST data were collected from three different regions of interest (the lower leg muscle, the olfactory bulb and the neocortex) of eight rats.

**Results:** The CEST effect for carnosine, anserine and homocarnosine was characterized in phantoms, demonstrating the possibility to separate individual contributions by employing high spectral resolution (0.005 ppm) and low CEST saturation power (0.15  $\mu$ T). The CEST signature of these peptides was evidenced, in vivo, in the rat brain and skeletal muscle. The presence of carnosine and anserine in the muscle was corroborated by in vivo localized spectroscopy (MRS). However, the sensitivity of MRS was insufficient for carnosine and homocarnosine detection in the brain. The absolute amounts of carnosine and derivatives in the investigated tissues were determined by liquid chromatography–electrospray ionization–tandem mass spectrometry using isotopic dilution standard methods and were in agreement with the CEST results.

**Conclusion:** The robustness of the CEST-linescan approach and the favorable conditions for CEST at ultra-high magnetic field allowed the in vivo CEST MR detection of carnosine and related peptides. This approach could be useful to investigate noninvasively the (patho)-physiological roles of these molecules.

## KEYWORDS

carnosine, chemical exchange saturation transfer, histidine dipeptides, in vivo MRS, mass spectrometry, ultra-high field

## 1 | INTRODUCTION

Chemical Exchange Saturation Transfer (CEST)<sup>1</sup> is a noninvasive method that has proved useful to detect low-concentrated endogenous metabolites with labile protons. Based on the exchange of protons between a metabolite of interest with bulk water, CEST provides an indirect detection of the considered metabolite with enhanced sensitivity compared to its direct detection using <sup>1</sup>H-NMR spectroscopy. In the last 10 years, CEST techniques have been widely applied to detect and map important metabolites such as glucose (glucoCEST),<sup>2</sup> glutamate (gluCEST),<sup>3</sup> or creatine (CrCEST),<sup>4</sup> as well as, less specifically, compounds possessing amide moieties (APT-CEST).<sup>5</sup> Yet, it remains challenging to investigate weaker CEST effects from molecules with low concentrations and slow exchange rates. In this study, we focus our attention on carnosine, for which the CEST detection has only been reported *in vitro*. Bodet et al.<sup>6</sup> have studied the CEST effect of carnosine in aqueous solutions (at a concentration of 50 mmol/L) and demonstrated that at 7 T, under physiological conditions (T = 37°C, pH = 7.1), carnosine can induce a CEST effect of about 1% (asymmetric magnetization transfer ratio) at approximately 3.1 ppm away from water.

Carnosine ( $\beta$ -alanyl-L-histidine) is a small endogenous dipeptide present in relatively high concentrations in several excitable tissues in mammals.<sup>7</sup> In particular, carnosine can be found in skeletal muscles (from 5 to 7 mmol/L in humans<sup>8</sup> and 3 to 5 mmol/L in rats<sup>9</sup>). In rodents, carnosine is present in the muscles together with a methylated derivative called anserine ( $\beta$ -alanyl-3-methylhistidine) whose concentration can reach even higher values.<sup>9</sup> Relatively large amounts of carnosine have also been reported in the olfactory bulb.<sup>10</sup> In the rest of the brain, the concentration of carnosine decreases below 0.2 mmol/L but another carnosine derivative is also present, homocarnosine ( $\gamma$ -amino-butyryl-histidine) at slightly higher concentrations ( $\approx$  0.5 mmol/L in the rat brain<sup>11</sup> and  $\approx$  0.3–0.4 mmol/L in the human brain<sup>12</sup>).

As carnosine, both anserine and homocarnosine have a labile proton capable of generating CEST effect (the amide proton of the peptide bond). Compared to other metabolites, such as glutamate or glucose, the exchange rate of carnosine is one order of magnitude lower,<sup>6</sup> which limits the attainable signal amplification through CEST and makes its indirect detection *in vivo* more challenging.

A conventional CEST acquisition consists in the recording of the water signal following the application of saturation pulses at varying saturation offsets (the so-called Z-spectrum). Such acquisitions are time-consuming and therefore prone to frequency drifts

and temperature fluctuations, resulting in poor signal stability over time, and compromised detection sensitivity. For this reason, in this study, we chose to use a fast acquisition approach which we call CEST-linescan (CEST-LS), that enables the acquisition of an entire Z-spectrum in only two scans. The CEST-LS pulse sequence was developed according to the ultrafast Z-spectrum (UFZ) methodology introduced by Xu et al.<sup>13,14</sup> and it is based on the application of magnetic field gradients during the saturation module resulting in the spatial encoding of the saturation frequency. Because it allows a dramatic reduction of the acquisition time, CEST-LS results in increased signal stability while maintaining a contrast-to-noise ratio similar to that of standard CEST sequences, which is particularly useful for *in vivo* applications.

Using the CEST-LS approach in combination with an ultra-high magnetic field (17.2 T), we demonstrate the detection of carnosine and its derivatives *in vivo*, in the brain and the skeletal muscle of healthy adult rats.

## 2 | METHODS

All phantom and *in vivo* CEST acquisitions were performed on a 17.2 T (<sup>1</sup>H Larmor frequency = 730.2 MHz) Bruker Biospec preclinical scanner equipped with a Bruker Avance III console running Paravision 6.0.1 (Bruker BioSpec) and a gradient system allowing a maximum gradient strength of 1 T/m. Phantom images were acquired using a 25-mm diameter quadrature bird-cage volume coil (Rapid Biomedical) while *in vivo* images were acquired using a receive surface coil (Rapid Biomedical) and a 45-mm diameter birdcage transmit volume coil (Rapid Biomedical).

### 2.1 | CEST-linescan pulse sequence

CEST data were acquired using a CEST-LS sequence developed for Paravision 6.0.1 starting from a standard gradient echo pulse sequence in which we deactivated the phase encoding gradient and added a CEST saturation module. Compared to the simplest implementation of the UFZ technique,<sup>13</sup> the CEST-LS sequence used here includes a slice selection gradient and outer-volume saturation bands (Figure 1), in order to limit the CEST acquisition to a given region-of-interest (ROI). The saturation module consists in saturation pulses applied on-resonance in the presence of a gradient. As a result, spins that are located along the direction of the gradient at a distance  $d$  from the isocenter will experience an irradiation at saturation offsets given by  $\gamma \times G_{\text{sat}} \times d$ , where  $\gamma$  is the gyromagnetic ratio and  $G_{\text{sat}}$  is the amplitude of the gradient. During the acquisition,

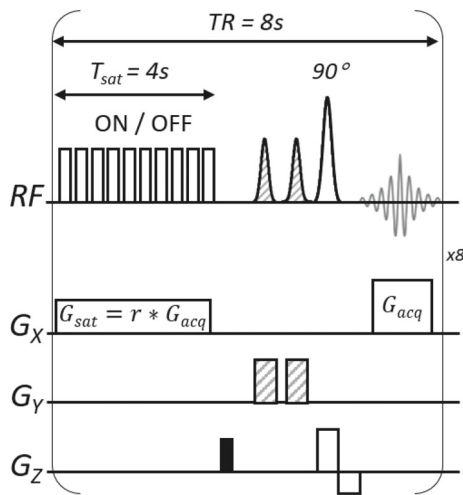


**FIGURE 1** The chemical exchange saturation transfer (CEST) saturation module was placed in front of a standard gradient echo sequence in which the phase encoding gradient was removed. Gradient spoilers were applied on the z direction (solid black rectangle). Field of view saturation bands were added to eliminate the signal outside the desired region-of-interest (hatch pattern). The CEST saturation pulses are switched ON and OFF (amplitude at zero) to generate saturated or reference profiles, respectively.

a gradient  $G_{acq}$  is applied along the same direction as the saturation gradient. The saturation range,  $BW_{sat}$ , is dictated by the acquisition bandwidth,  $BW_{acq}$ , and the ratio between the saturation gradient  $G_{sat}$  and the acquisition gradient  $G_{acq}$ :

$$r = \frac{G_{sat}}{G_{acq}} = \frac{BW_{sat}}{BW_{acq}}$$

It follows that, for an acquisition of  $N$  points, the apparent spectral discrimination, equivalent to the saturation frequency increment in conventional Z-spectra and referred to as CEST spectral resolution, is given by  $(r \times BW_{acq})/N$ .

To compensate for the irregular one-dimensional profile along the encoding direction, a second profile is acquired, with the saturation pulse turned off (corresponding to the proton density distribution along the line). The ratio between the saturated profile over the unsaturated profile gives a normalized Z-spectrum.

## 2.2 | CEST phantom experiments

The phantom studied was a 2.5 ml syringe filled with a mixture of 10 mmol/L carnosine, 10 mmol/L anserine and 20 mmol/L homocarnosine in 0.01 mol/L phosphate-buffered saline with the pH adjusted to 7.2. Carnosine and anserine were purchased from Sigma-Aldrich and homocarnosine from Cayman Chemical. During MR

acquisitions the syringe was maintained at 37°C using a feedback controlled air heating system.

For all CEST acquisitions, the saturation module consisted in 10 rectangular pulses of 400 ms duration, separated by a 0.01 ms delay. Z-spectra were acquired in a  $8 \times 9 \times 5 \text{ mm}^3$  ROI using saturation  $B_{1,sat}$  powers ranging between 0.15 and 1  $\mu\text{T}$ . Two different spectral resolutions were used: 0.03 ppm and 0.005 ppm, corresponding to ratios  $r$  of 0.05 and 0.01, respectively.

## 2.3 | In vivo experiments

Eight male adult Dark Agouti rats (200-300 g, Janvier Labs) were used in this study. This strain has been selected because Agouti rats are known to present higher amounts of carnosine and anserine.<sup>7</sup> The animals were housed by pair under a 12-h night/12-h daylight cycle with water and food available ad libitum. All animal procedures were approved by the Comité d'Éthique en Expérimentation Animale, Commissariat à l'Énergie Atomique et aux Énergies Alternatives, and by the Ministère de l'Éducation Nationale, de l'Enseignement Supérieur et de la Recherche (France) under reference A15 – 40 and were conducted in strict accordance with the recommendations and guidelines of the European Union (Directive 2010/63/EU) and the French National Committee (Décret 2013–118).

During all MRI exams, an air-oxygen mixture (2:1) was continuously delivered to the animals through a nose-cone mask. For induction, isoflurane was maintained at 3% for 3 min, then lowered to 1.5–2% and adjusted throughout the experiment to maintain the respiration rate at around 60 breaths/min. The body temperature was kept between 36 and 38°C using a heated water circulation system. The respiration and body temperature were monitored using a small animal monitoring system (SA Instruments Inc.).

For each exam, an anatomical  $T_2$ -weighted reference image was acquired to help positioning the CEST-LS ROI (Figure 3A). Local  $B_0$  field homogenization was performed prior to the CEST-LS acquisitions using an automatic shimming routine. All CEST-LS acquisitions were performed with  $TE/TR = 3/8000 \text{ ms}$  (with negligible  $T_1$  or  $T_2^*$  weightings) and a saturation power of 1  $\mu\text{T}$ . Other parameters varied depending on the investigated region and are detailed in Table 1. Eighty repetitions (pairs of CEST-LS datasets with and without the saturation module) were acquired to increase the SNR for a total acquisition time of 21m20s.

Additionally, single-voxel  $^1\text{H-NMR}$  spectra were acquired using a LASER sequence<sup>15</sup> ( $TE/TR = 25/3000 \text{ ms}$ , 256 averages, 8 kHz acquisition bandwidth, 1024

**TABLE 1** Parameters used for in vivo Z-spectra generated with CEST-LS.  $r$  is the ratio between the saturation gradient  $G_{\text{sat}}$  and the acquisition gradient  $G_{\text{acq}}$ . Please note that the spectral resolution is given after zero-filling with a factor of 2. In the manuscript, only zero-filled data are shown, and zero-filled spectral resolutions are given.

Investigated region	Muscle		Olfactory bulb		Neocortex	
CEST-LS ROI dimension (mm <sup>3</sup> )	9 × 4 × 2		4 × 1.8 × 2.5		7 × 3 × 2	
Z-spectrum	Full	Zoom	Full	Zoom	Full	Zoom
Ratio $r$	0.15	0.05	0.15	0.07	0.15	0.07
Saturation range (ppm)	10.3	3.4	10.3	4.8	10.3	4.8
Spectral resolution after zero-filling (ppm)	0.08	0.03	0.08	0.04	0.08	0.04

points) from a  $3 \times 1.8 \times 1.5$  mm<sup>3</sup> voxel placed at the center of the CEST-LS ROI (Figure 3A). Water suppression was achieved using VAPOR.<sup>16</sup>

## 2.4 | LC-ESI-MS/MS

Olfactory bulb, brain (devoid of olfactory bulb and cerebellum) and skeletal leg muscle (gastrocnemius) tissues were weighted and homogenized at a wet weight:volume ratio of 100 mg tissue:ml of HCOONH<sub>4</sub> at 100 mM, pH 4 at 4°C with a Bead Bug tissue homogenizer (Benchmark Scientific) for 2 min at 4000 rpm. The samples obtained were centrifuged at 4°C for 10 min at 14 000 rpm and the supernatant stored at −80°C until the analysis. Samples for LC-MS analyses were prepared by diluting 20 μl of tissue supernatants with 180 μl of acetonitrile for olfactory bulb and muscle and 80 μl for brain; acetonitrile was spiked with [<sup>13</sup>C3]-carnosine used as internal standard (IS), synthesized as described by Maspero et al.,<sup>17</sup> to reach a 1 μM final concentration. The samples were kept in ice for 20 min and centrifuged at 4°C for 10 min at 14 000 rpm. Aliquots of 100 μl of the supernatant were transferred to vials containing 100 μl of acetonitrile spiked with increasing concentration of carnosine, anserine (Flamma s.p.a., Chignolo D'isola) and homocarnosine (Sigma) to reach the following final concentrations; 0, 1, 2, 3, and 4 μM. Before transfer in vials for the analysis the samples were vortexed for 30 s. Each sample was prepared in triplicate and injected once in a randomized way.

The analyses were performed on an ExionLC-100 coupled to an API4000 equipped with a Turbo-V ESI source (AB-Sciex) using the same chromatographic conditions as reported by Maspero et al.<sup>17</sup> with the following modification: mobile phase A was HCOONH<sub>4</sub> 100 mM at pH = 4 instead of pH = 3. The mass spectrometer was set to acquire in multiple reaction monitoring mode using the transitions reported in Supporting Information Table S1 and identical source parameters as in Maspero et al.<sup>17</sup> The instrument control was carried out with Analyst (version 1.6.3; AB-Sciex).

## 2.5 | Data analysis

### 2.5.1 | CEST-LS

All CEST-LS data were analyzed using in-house written MATLAB scripts (Mathworks, version 9.7, R2019b). To obtain the Z-spectra, CEST data were processed as follows: after a zero-filling which doubled the number of FID data points (from 64 to 128), the ratio between the Fourier transform of the signal acquired with and without saturation was plotted against the saturation frequency offsets. The chemical shifts of the Z-spectrum were corrected using a cubic spline data interpolation in order to center the water peak on 0 ppm. For higher resolution Z-spectra, not covering the water peak, the chemical shift correction was performed using other known, major peaks: phosphocreatine at 2.6 ppm in the muscle and creatine at 2 ppm in the olfactory bulb and neocortex.

The in vivo Z-spectra were analyzed using a Python-based algorithm (PEAKIT)<sup>18</sup> able to detect, calculate heights and areas and evaluate the significance of CEST peaks. For the skeletal muscle, only the significance of the carnosine + anserine peak was assessed while for the olfactory bulb and cortex, the areas of carnosine, homocarnosine and APT peaks were also determined. The area of the APT peak was calculated over a range of 2.8 ppm and centered on the peak maximum, as found by PEAKIT. For the carnosine and homocarnosine peaks, the range for area calculation was automatically selected by PEAKIT. PEAKIT is freely available from <https://github.com/SKMikee/PeakIt>.

### 2.5.2 | MRS

Following removal of the residual water signal using the Hankel Lanczos singular value decomposition (HLSVD) algorithm, in vivo <sup>1</sup>H-NMR spectra were processed over the [0.5–9] ppm range using LCModel 6.2.<sup>19</sup> The basis set of metabolite spectra was simulated using a spin

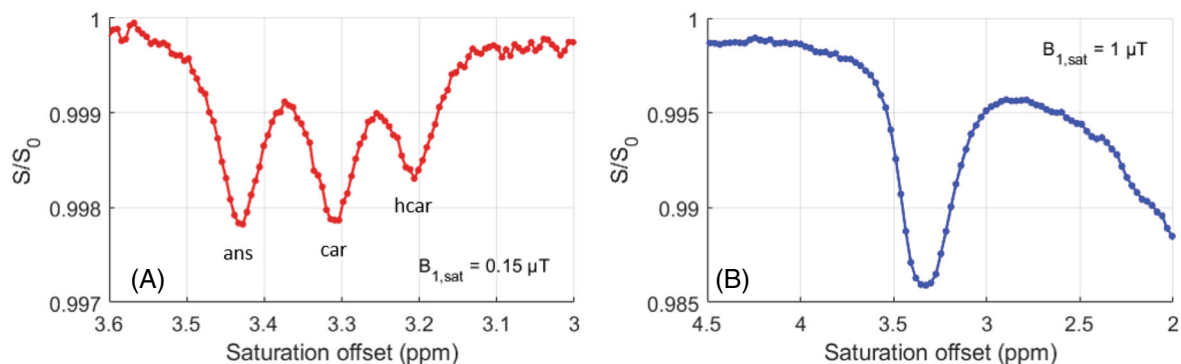


**FIGURE 2** (A) CEST-LS Z-spectrum obtained with  $B_{1,sat}$  0.15  $\mu$ T and a resolution of 0.005 ppm. Homocarnosine, carnosine and anserine peaks are clearly visible and distinct. (B) CEST-LS Z-spectrum obtained with  $B_{1,sat}$  1  $\mu$ T and a resolution of 0.03 ppm. The Z-spectra in A and B were averaged over 10 and 18 repetitions, respectively. We note that in,<sup>6</sup> the CEST effect of carnosine was reported at 3.1 ppm which is slightly different from our results. This is most likely due to slight differences in pH.

simulation software implemented in Matlab and based on the density matrix formalism.

### 2.5.3 | LC-ESI-MS/MS

The calibration curves were built for each analyzed sample by using a standard addition method. The peak area ratios of analyte/IS were plotted versus the nominal concentrations of genuine carnosine, anserine and homocarnosine spiked in the sample to reach the following final concentrations: 0, 1, 2, 3, and 4  $\mu$ M. Weighted ( $1/\times 2$ ) least-squares linear regressions were calculated by using the software GraphPad Prism. The calculated analyte concentration was then reported as moles per gram of wet tissue on the basis of the weight of the wet tissue and serial dilutions.

## 3 | RESULTS

### 3.1 | In vitro study

Figure 2 shows representative Z-spectra acquired on the mixture sample with  $B_{1,sat}$  of 0.15  $\mu$ T and spectral resolution 0.005 ppm (Figure 2A) and  $B_{1,sat}$  of 1  $\mu$ T and spectral resolution 0.03 ppm (Figure 2B). The very low  $B_{1,sat}$  of 0.15  $\mu$ T coupled with a very high spectral resolution (0.005 ppm) allowed to accurately separate and detect the CEST effects of homocarnosine (hcar), carnosine (car) and anserine (ans) at  $3.20 \pm 0.01$  ppm,  $3.31 \pm 0.01$  ppm and  $3.43 \pm 0.01$  ppm, respectively. These parameters did not, however, give satisfactory results in vivo due to the low contrast-to-noise ratio. Moreover, we aimed at covering a range of frequencies sufficiently large to encompass reference peaks such as creatine or phosphocreatine, which set

a higher bound for the resolution at 0.03 ppm (see next section). We therefore used  $B_{1,sat}$  of 1  $\mu$ T and a spectral resolution equal or lower than 0.03 ppm for all in vivo acquisitions. Figure 2B shows the CEST-LS Z-spectrum obtained on the mixture sample with  $B_{1,sat}$  of 1  $\mu$ T and spectral resolution of 0.03 ppm. The larger bandwidth corresponding to the higher  $B_{1,sat}$  power did not allow the separation of the three peptides. We conclude therefore that in vivo one cannot distinguish between carnosine, anserine and homocarnosine.

### 3.2 | In vivo study

#### 3.2.1 | Skeletal muscle

The position of the CEST-LS acquisition is depicted by the orange ROI shown on the anatomical image of a rat lower-leg in Figure 3A. Figure 3B shows an example of a Z-spectrum (spectral resolution 0.08 ppm) acquired in the orange rectangle in Figure 3A, in which we can recognize the creatine (Cr) and phosphocreatine (PCr) CEST peaks on the left, as well as a broad peak corresponding to the NOE effect from aliphatic protons (Nuclear Overhauser Enhancement) on the right. Figure 3C shows a higher spectral resolution Z-spectrum (0.03 ppm resolution) which was acquired using a weaker CEST saturation gradient ( $r = 0.05$  vs. 0.15). The Cr and PCr peaks are more evident at higher spectral resolution. Moreover, two additional peaks corresponding to the combination of carnosine and anserine at  $3.32 \pm 0.06$  ppm and APT at  $3.5 \pm 0.06$  ppm are also visible.

Similar results were obtained on four different animals. The analyses performed with PEAKIT confirmed the significance of all carnosine + anserine peaks ( $p < 0.05$ ).

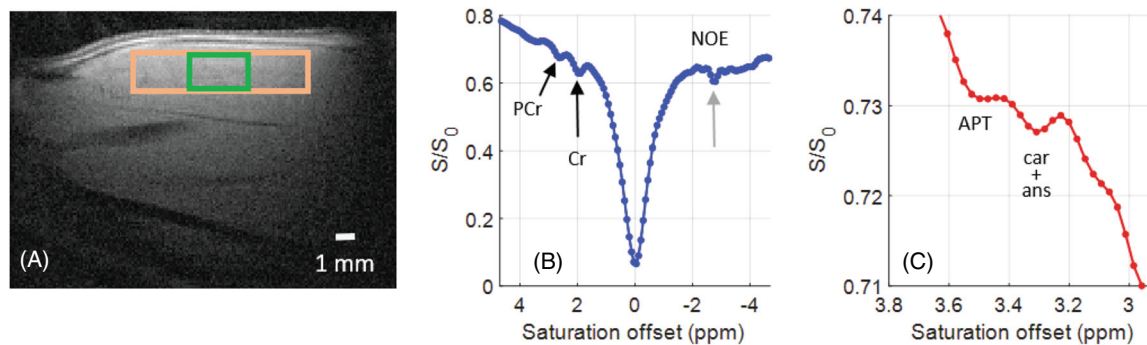


**FIGURE 3** (A) Anatomical image of a rat lower-leg muscle showing the ROI used for CEST-LS in orange and the voxel for  $^1\text{H-NMR}$  spectroscopy in green. (B) Low resolution Z-spectrum showing the Creatine (Cr) and PhosphoCreatine (PCr). The sharp peak indicated by a gray arrow at -2.7 ppm corresponds to fat<sup>20</sup> (C) Zoom showing combined car + ans and APT peaks. All Z-spectra were acquired with  $B_{1,\text{sat}} = 1 \mu\text{T}$ .

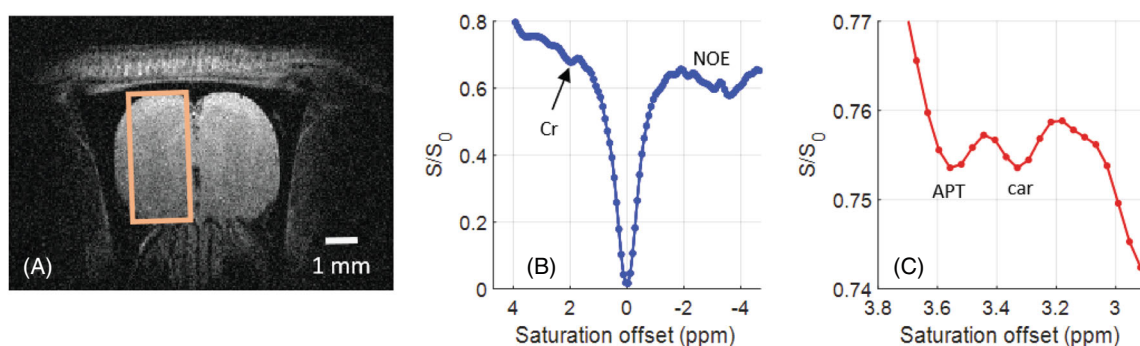


**FIGURE 4** (A) Anatomical image of a rat olfactory bulb showing the region-of-interest used for the CEST-LS acquisitions; (B) Low-resolution Z-spectrum showing the Cr peak (C) High resolution Z-spectrum showing car and APT peaks. All Z-spectra were acquired with  $B_{1,\text{sat}} = 1 \mu\text{T}$ .

### 3.2.2 | Olfactory bulb

As the olfactory bulb is a relatively small region, the ROIs chosen for the CEST-LS acquisitions were smaller than in the leg (Figure 4A and Table 1). The Z-spectrum in Figure 4B shows clearly a peak at 2 ppm, as well as a shoulder at 2.6 ppm corresponding to Cr and PCr, respectively. By increasing the spectral resolution to 0.04 ppm (Figure 4C), we put in evidence the APT peak at 3.5 ppm. Close to it, the carnosine peak is recognizable. Note that the spectral resolution for the Z-spectrum in Figure 4C is slightly lower than that for the leg muscle to compensate for the lower signal-to-noise ratio due to the smaller ROI size. Similar results were obtained in four animals with the significance for the carnosine peak confirmed by PEAKIT ( $p < 0.05$ ). The average ratio of the carnosine to the APT peak areas was found  $0.51 \pm 0.31$ .

### 3.2.3 | Neocortex

Finally, the last set of experiments was performed in the neocortex. Despite a lower histidine dipeptides expected

concentration,<sup>9</sup> the larger size of this brain structure and the better  $B_0$  homogeneity compared to the olfactory bulb were beneficial to the SNR of these experiments. On the low resolution Z-spectrum (Figure 5B) acquired in the orange ROI in Figure 5A we recognize the 2 ppm Cr peak.<sup>21</sup> The zoom on the high resolution Z-spectrum (Figure 5B) shows a broad APT peak as well as a local decrease around 3.2 ppm which corresponds to the CEST contribution of homocarnosine. The homocarnosine peaks were detected with a p-value below 0.05 using PEAKIT for all four animals scanned. The average ratio of the homocarnosine to the APT peak areas was found  $0.21 \pm 0.06$ , which is 2.4 times lower than the carnosine/APT ratio found in the olfactory bulb.

### 3.2.4 | In vivo direct spectroscopy

The  $^1\text{H-NMR}$  spectra of carnosine and carnosine derivatives samples show two distinct resonances downfield from water at chemical shifts 7.08 and 8.08 ppm, corresponding to the C4 and C2 histidine-imidazole protons, respectively. These two resonances are easily identifiable

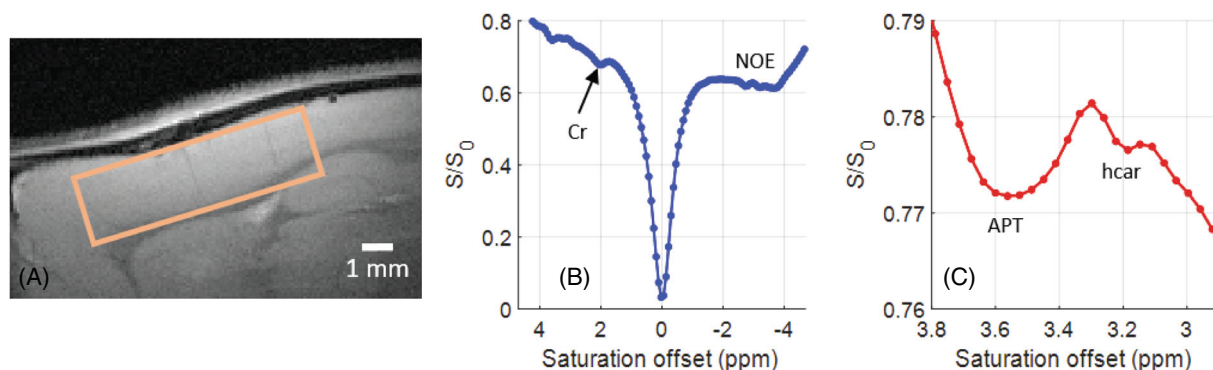


**FIGURE 5** (A) Anatomical image of a rat neocortex showing the region-of-interest used for the CEST-LS acquisitions. (B) Low-resolution Z-spectrum showing the Cr peak. (C) High-resolution Z-spectrum showing the hcar and APT peaks. All Z-spectra were acquired with  $B_{1,sat}=1 \mu\text{T}$ .

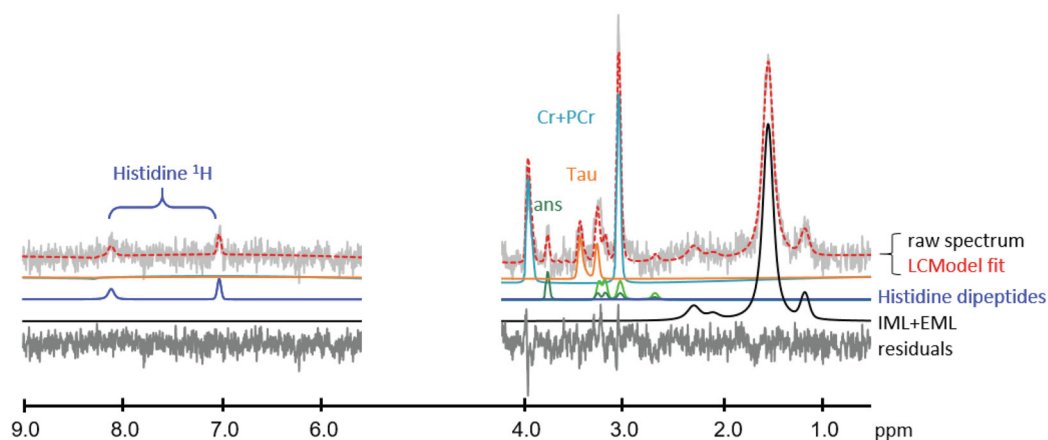


**FIGURE 6** In vivo NMR spectrum acquired on a  $3 \times 1.8 \times 1.5 \text{ mm}^3$  voxel in the leg skeletal muscle (green box in Figure 3A). Peaks at approximately 7.08 and 8.08 ppm are the signature of both carnosine and anserine (labeled Histidine dipeptides and represented in blue) while the peak at 3.7 ppm is proper to anserine (dark green). The light green line on the right represents carnosine.

on the spectrum in Figure 6, which was obtained in the green voxel showed in Figure 3A, confirming the presence of carnosine and anserine in the leg skeletal muscle. From the decomposition of the  $^1\text{H}$ -NMR spectra using the LCModel,<sup>19</sup> we estimate an average ( $N = 4$  animals) of total carnosine concentration of  $(8.4 \pm 0.5) \text{ mmol/L}$  considering a Cr+PCr concentration of 38 mmol/L.

For the olfactory bulb and the neocortex,  $^1\text{H}$ -MRS did not allow the detection of neither carnosine nor homocarnosine. The heterogeneity and the small size of the olfactory bulb as well as the low concentration expected in the neocortex may explain why we were below the limit of detection in both cases.

### 3.2.5 | LC-ESI-MS/MS

The calibration curves built for each sample were linear for all the three analytes (carnosine, anserine, and

homocarnosine) with  $R^2$  from 0.8990 to 0.9689 for the olfactory bulb, 0.8821 to 0.9636 for the muscle, and 0.9535 to 0.9845 for the brain. The extrapolated concentrations of the three dipeptides were calculated for each sample, and the results expressed as nmoles of dipeptide contained in 1 g of wet tissue. Table 2 reports the mean  $\pm$  SD of carnosine, anserine and homocarnosine in the rat tissues. Anserine is the most abundant histidine dipeptide in skeletal muscle, with a concentration of almost 36% higher than carnosine while homocarnosine was not detected. The olfactory bulb contains only carnosine while anserine and homocarnosine were both undetectable. Homocarnosine was the most abundant peptide in the brain with a content almost three time higher than that of carnosine while anserine was not detected. Table 2 also reports the total amount of histidine dipeptides calculated as the sum of carnosine + anserine + homocarnosine. The skeletal muscle is the tissue characterized by the highest amount of histidine dipeptides with a content almost

**TABLE 2** Carnosine, anserine, homocarnosine and total histidine dipeptides concentrations found in the muscle, olfactory bulb and brain. The values are averaged over four rats and reported as nmoles of dipeptide per gram of wet tissue  $\pm$  SD.

	Concentration (nmoles/g of wet tissue)			
	Carnosine	Anserine	Homocarnosine	Histidine dipeptides
Muscle	2262.2 $\pm$ 1254.7	3518.5 $\pm$ 774.6	N.D.	5780
Olfactory bulb	447.5 $\pm$ 116.0	N.D.	N.D.	447.5
Brain	55.7 $\pm$ 18.4	N.D.	168.9 $\pm$ 39.9	224.6

Abbreviation: N.D., not detected.

13 and 25 folds higher than that of the bulb and brain, respectively.

## 4 | DISCUSSION AND CONCLUSIONS

In this study, we demonstrate the *in vivo* detection of carnosine and its derivatives in rats using CEST. This was accomplished by using a custom designed fast CEST acquisition, CEST-LS, in combination with an ultra-high magnetic field (17.2 T) imaging system. The characterization of the CEST effect was performed using the PEAKIT software,<sup>18</sup> which makes a local estimation of the baseline and therefore reduces the contamination from other broad CEST signals (e.g. taurine, glutamine, glutamate in the brain<sup>22</sup>) improving the detection selectivity of the technique. We cannot however, completely exclude any signal contamination from other metabolites or peptides if present. The presence of carnosine and derivatives was validated in the leg with direct NMR spectroscopy *in vivo* but was not possible for the olfactory bulb and the neocortex. This confirms that, under our experimental conditions, CEST is a more sensitive approach than localized MRS.

Moreover, by optimizing the CEST-LS acquisition parameters we were able to disentangle the contributions of carnosine, anserine and homocarnosine in a phantom sample. This was, however, not possible *in vivo* due to the low CEST effect achieved with the saturation powers employed for *in vitro* acquisitions (0.15  $\mu$ T) and the presence of other CEST contributions.

The LC-ESI-MS/MS quantification of carnosine, anserine and homocarnosine reports a content of histidine dipeptides of more than 13 and 25 times higher in the skeletal muscle than in the olfactory bulb and brain, respectively. These data explain well the <sup>1</sup>H-MRS results and in particular the fact that the technique is not able to detect these peptides in the olfactory bulb and in the neocortex. According to the LC-ESI-MS/MS analysis the concentration of carnosine in the olfactory bulb is approximately 2.6 times higher than the homocarnosine concentration found

in the rest of the brain. These results are in agreement with CEST-LS data, which, taking into account the area ratio carnosine/APT for the olfactory bulb and homocarnosine/APT for the neocortex as an index of the relative histidine dipeptide content indicate a 2.4 times higher concentration in the olfactory bulb.

Although some of its physiological functions are still being investigated, it has been clearly established that carnosine presents direct and indirect antioxidant activity through its ability to scavenge free radicals,<sup>23,24</sup> inhibit protein carbonylation and glycoxylation,<sup>25,26</sup> and chelate metallic ions.<sup>27</sup> Carnosine was suggested to be involved in various biochemical processes, including pH-buffering in the muscle<sup>28</sup> and Ca<sup>2+</sup> regulation.<sup>29</sup> Tiedje et al.<sup>30</sup> have also presented carnosine as an important neurotransmitter in the olfactory bulb. Homocarnosine is seen in long range projecting GABAergic neurons<sup>31</sup> and appears to possess anticonvulsant properties as well as to play a role in modulating cortical excitability.<sup>32,33</sup> Despite this, there are very few human study reports of *in vivo* homocarnosine/carnosine detection using MRS<sup>12,34-36</sup> and, to our knowledge, none using CEST. This is nevertheless due to the low concentrations at which these metabolites are present in the brain. CEST approaches as the one presented in this manuscript could potentially be extended to human studies. The optimal B<sub>1,sat</sub> power for *in vivo* carnosine detection is relatively low at 1  $\mu$ T, and therefore compatible with the specific absorption rate constraints imposed for human brain investigations. Carnosine presents a CEST contribution at 3.3 ppm away from water and therefore its detection is only moderately affected by direct water saturation with the considered B<sub>1,sat</sub> values. Numerical simulations performed at 11.7, 7, and 3 T show a carnosine CEST effect decrease by 8, 23, and 48%, respectively, compared to that at 17.2 T (Supporting Information Figure S1). This decrease combined with the close proximity of other CEST contributions such as glutamate at 3 ppm and APT at 3.5 ppm will make the *in vivo* detection of carnosine and derivatives at lower magnetic fields more challenging. Further investigations are necessary in order to assess whether ultra high magnetic field scanners (from 7 up to 11.7 T)



available today for human imaging would allow the CEST detection of homocarnosine/carnosine in the human brain or anserine/carnosine in the skeletal muscle.

While the CEST-linescan strategy presented here offers the great advantage of being minimally affected by temporal variations in frequency, temperature, or physiological parameters, it has the local nature of the detection as main limitation. It should be noted, however, that the technique does not require a homogeneous sample along the gradient direction for accurate local measurements, as the signal is normalized by the reference signal at each position acquired in the absence of saturation. This normalization procedure also makes the CEST-LS technique less susceptible to  $B_0$  inhomogeneities compared to standard CEST approaches. In the current study, we used the water peak or other known CEST peaks to find the chemical shift offset of the peaks under study. The precision of such referencing can be affected by large  $B_0$  fluctuations, which can however be corrected by acquiring a  $B_0$  map in the CEST-LS ROI. The implementation of such correction step is underway. We note that a similar approach, ultrafast localized CEST-spectroscopy with PRESS,<sup>37</sup> has been previously used for performing CEST acquisitions in the human brain at 3 T. Compared to ultrafast localized CEST-spectroscopy with PRESS, our CEST-LS approach offers more flexibility in the choice of the acquisition parameters, allowing for shorter echo times.

To conclude, despite the low CEST effect exhibited by carnosine and its derivatives, we show the possibility of their *in vivo* detection, both in the skeletal muscle and in the brain using CEST-LS. We propose this approach for the detection of other low concentrated metabolites both in preclinical and clinical settings at high magnetic fields.


## ACKNOWLEDGMENTS

This research was supported by a public grant overseen by the ANR (France) and DFG (Germany) under the project name BAMBOO (ANR-18-CE92-0054-01). The authors thank T. Delebarre for assistance with the numerical simulations and E. Selingue for support with the animal preparation and welfare.

## ORCID

Solène Bardin  <https://orcid.org/0000-0001-5009-1658>

Michele Lecis  <https://orcid.org/0000-0001-8418-3198>

Giovanna Baron  <https://orcid.org/0000-0002-9335-6318>

Luisa Ciobanu  <https://orcid.org/0000-0001-6932-6859>

## REFERENCES

1. Wolff SD, Balaban RS. NMR imaging of labile proton exchange. *J Magn Reson.* 1990;86:164-169.
2. Chan KW, McMahon MT, Kato Y, et al. Natural D -glucose as a biodegradable MRI contrast agent for detecting cancer. *Magn Reson Med.* 2012;68:1764-1773.
3. Cai K, Haris M, Singh A, et al. Magnetic resonance imaging of glutamate. *Nat Med.* 2012;18:302-306.
4. Pavuluri KD, Rosenberg JT, Helsper S, Bo S, McMahon MT. Amplified detection of phosphocreatine and creatine after supplementation using CEST MRI at high and ultrahigh magnetic fields. *J Magn Reson.* 2020;313:106703.
5. Zhou J, Lal B, Wilson DA, Larterra J, van Zijl PC. Amide proton transfer (APT) contrast for imaging of brain tumors. *Magn Reson Med.* 2003;50:1120-1126.
6. Bodet O, Goerke S, Behl NG, Roeloffs V, Zaiss M, Bachert P. Amide proton transfer of carnosine in aqueous solution studied *in vitro* by WEX and CEST experiments. *NMR Biomed.* 2015;28:1097-1103.
7. Boldyrev AA, Aldini G, Derave W. Physiology and pathophysiology of carnosine. *Physiol Rev.* 2013;93:1803-1845.
8. Krššák M, Lindeboom L, Schrauwen-Hinderling V, et al. Proton magnetic resonance spectroscopy in skeletal muscle: experts' consensus recommendations. *NMR Biomed.* 2020;34:1-20.
9. Aldini G, Facino RM, Beretta G, Carini M. Carnosine and related dipeptides as quenchers of reactive carbonyl species: from structural studies to therapeutic perspectives. *Biofactors.* 2005;24:77-87.
10. Bonfanti L, Peretto P, De Marchis S, Fasolo A. Carnosine-related dipeptides in the mammalian brain. *Prog Neurobiol.* 1999;59:333-353.
11. O'Dowd JJ, Cairns MT, Trainor M, Robins DJ, Miller J. Analysis of carnosine, homocarnosine, and other histidyl derivatives in rat brain. *J Neurochem.* 1990;55:446-452.
12. Landheer K, Prinsen H, Petroff OA, Rothman DL, Juchem C. Elevated homocarnosine and GABA in subject on isoniazid as assessed through <sup>1</sup>H MRS at 7T. *Anal Biochem.* 2020;599:113738.
13. Xu X, Lee JS, Jerschow A. Ultrafast scanning of exchangeable sites by NMR spectroscopy. *Angew Chem.* 2013;125:8439-8442.
14. Boutin C, Léonce E, Brotin T, Jerschow A, Berthault P. Ultrafast z-spectroscopy for <sup>129</sup>Xe NMR-based sensors. *J Phys Chem Lett.* 2013;4:4172-4176.
15. Garwood M, Delabarre L. The return of the frequency sweep: designing adiabatic pulses for contemporary NMR. *J Magn Reson.* 2001;153:155-177.
16. Tkáč I, Starčuk Z, Choi IY, Gruetter R. *In vivo* <sup>1</sup>H NMR spectroscopy of rat brain at 1 ms echo time. *Magn Reson Med.* 1999;41:649-656.
17. Maspero M, Gilardoni E, Bonfanti C, et al. Synthesis and characterization of <sup>13</sup>C labeled carnosine derivatives for isotope dilution mass spectrometry measurements in biological matrices. *Talanta.* 2021;235:122742.
18. Lecis M, Bardin S, Ciobanu IC, Ciobanu L. PEAKIT: a Gaussian process regression analysis tool for chemical exchange saturation transfer spectra. *J Magn Reson.* 2021;334:107122.
19. Provencher SW. Estimation of metabolite concentrations from localized *in vivo* proton NMR spectra. *Magn Reson Med.* 1993;30:672-679.
20. Triplett WT, Baligand C, Forbes SC, et al. Chemical shift-based MRI to measure fat fractions in dystrophic skeletal muscle. *Magn Reson Med.* 2014;72:8-19.

21. Cai K, Singh A, Poptani H, et al. CEST signal at 2ppm (CEST at 2ppm) from Z-spectral fitting correlates with creatine distribution in brain tumor. *NMR Biomed*. 2015;28:1-8.
22. Khlebnikov V, van der Kemp WJM, Hoogduin H, Klomp DWJ, Prompers JJ. Analysis of chemical exchange saturation transfer contributions from brain metabolites to the Z-spectra at various field strengths and pH. *Sci Rep*. 2019;1:1-11.
23. Kohen R, Yamamoto Y, Cundy KC, Ames BN. Antioxidant activity of carnosine, homocarnosine, and anserine present in muscle and brain. *Proc Natl Acad Sci*. 1988;85:3175-3179.
24. Boldyrev AA, Dupin AM, Pindel EV, Severin SE. Antioxidative properties of histidine-containing dipeptides from skeletal muscles of vertebrates. *Compar Biochem Physiol B*. 1988;89:245-250.
25. Hipkiss AR. Energy metabolism, proteotoxic stress and age-related dysfunction - protection by carnosine. *Mol Aspects Med*. 2011;32:267-278.
26. Aldini G, De Courten B, Regazzoni L, et al. Understanding the antioxidant and carbonyl sequestering activity of carnosine: direct and indirect mechanisms. *Free Radic Res*. 2020;55:321-330.
27. Brown CE, Antholine WE. Chelation chemistry of carnosine. Evidence that mixed complexes may occur in vivo. *J Phys Chem*. 1979;83:3314-3319.
28. Harris RC, Tallon MJ, Dunnett M, et al. The absorption of orally supplied  $\beta$ -alanine and its effect on muscle carnosine synthesis in human vastus lateralis. *Amino Acids*. 2006;30:279-289.
29. Dutka TL, Lambole CR, McKenna MJ, Murphy RM, Lamb GD. Effects of carnosine on contractile apparatus Ca<sup>2+</sup> sensitivity and sarcoplasmic reticulum Ca<sup>2+</sup> release in human skeletal muscle fibers. *J Appl Physiol*. 2012;112:728-736.
30. Tiedje KE, Stevens K, Barnes S, Weaver DF.  $\beta$ -alanine as a small molecule neurotransmitter. *Neurochem Int*. 2010;57:177-188.
31. Kish SJ, Perry TL, Hansen S. Regional distribution of homocarnosine, homocarnosine-carnosine synthetase and homocarnosinase in human brain. *J Neurochem*. 1979;32:1629-1636.
32. Petroff O. Williamson a homocarnosine enhances inhibitory tone in rat hippocampus. *Ann Neurol*. 2009;66:S14.
33. Williamson A, Petroff O, Spencer D. Homocarnosine effects on synchronous activity in the human hippocampus. *Epilepsia*. 2007;48:248-380.
34. Vermathen P, Capizzano AA, Maudsley AA. Administration and 1H MRS, detection of histidine in human brain: application to in vivo pH measurement. *Magn Reson Med*. 2000;43:665-675.
35. Solis MY, Cooper S, Hobson RM, et al. Effects of beta-alanine supplementation on brain homocarnosine/carnosine signal and cognitive function: an exploratory study. *PLoS One*. 2015;10:1-16.
36. Rothman DL, Behar KL, Prichard JW, Petroff OAC. Homocarnosine and the measurement of neuronal pH in patients with epilepsy. *Magn Reson Med*. 1997;38:924-929.
37. Liu Z, Dimitrov IE, Lenkinski RE, Hajibeigi A, Vinogradov E. UCEPR: ultrafast localized CEST-spectroscopy with PRESS in phantoms and in vivo. *Magn Reson Med*. 2016;75:1875-1885.

## SUPPORTING INFORMATION

Additional supporting information may be found in the online version of the article at the publisher's website.

**Table S1** MRM transitions for carnosine, anserine, homocarnosine and L-carnosine <sup>13</sup>C3.

**Figure S1** Simulated MTR<sub>asym</sub> for a 10 mM carnosine solution at four different B<sub>0</sub> magnetic fields: 3 T, 7 T, 11.7 T and 17.2 T. The Bloch-McConnell equations were solved using a twopool exchange model and employing the Matlab tool "CEST sources" available at [www.cestsources.org](http://www.cestsources.org). For simulations, the relaxation parameters of gray matter water were taken to be T<sub>1</sub> = 1, 1.7, 2.1, 2.3 s and T<sub>2</sub> = 0.08, 0.055, 0.035, 0.03 s for B<sub>0</sub> = 3, 7, 11.7, 17.2 T, respectively.

**How to cite this article:** Bardin S, Lecis M, Boido D, et al. In vivo detection of carnosine and its derivatives using chemical exchange saturation transfer. *Magn Reson Med*. 2022;88:1314-1323. doi: 10.1002/mrm.29282